UC Santa Cruz

UC Santa Cruz Previously Published Works

Title

Trace Key Mechanistic Features of the Arsenite Sequestration Reaction with Nanoscale
Zerovalent Iron

Permalink

https://escholarship.org/uc/item/9zj8x92r

Journal

Journal of the American Chemical Society, 143(40)

ISSN

0002-7863

Authors

Kao, Li Cheng
Ha, Yang
Chang, Wan-Jou
et al.

Publication Date

2021-10-13

DOI

10.1021/jacs.1c06159

Copyright Information

Peer reviewed

Trace Key Mechanistic Features of the As-nZVI Sequestration Reaction

Li Cheng Kao, Yang Ha, Wan Jou Chang, Xuefei Feng, Yifan Ye, Jeng-Lung Chen, Chih-Wen Pao, Feipeng Yang, Catherine Zhu, Wanli Yang, Jinghua Guo*, Sofia Ya Hsuan Liou*

Abstract

Nanoscale zerovalent iron (nZVI) is commonly used in advanced groundwater remediation processes. It is considered a highly efficient material for sequestrating arsenite, but the chemical transformations of arsenite and the reasoning for its high efficacy is not well understood. Here, we present a real-time monitoring method to investigate the complex mechanism of nZVI reaction *in situ,* with arsenite under anaerobic conditions at the time scale from seconds to days. The time-resolved XAS analysis recorded the dynamic changes of arsenic valence states at a mid-term stage (min to hours), showing an oxidation of As^{III} to As^{V}. This occurred both in the solid and liquid phase for the high nZVI dose system. When the reaction time increased up to 60 days, As^{V} became the dominant species and the As^{III} / As^{V} ratio of arsenic-laden nanoparticles, calculated by LCF, decreased to ca. 0.6. The oxygen K-edge mRIXS reveals that hybridization bonds enhanced with increasing reaction time, indicating the system is oxidizing upon. Although there is arsenic with a reduction character at the highest dose system, the reductive arsenic most likely formed on the solid/liquid interface and can be oxidized to As^{V} to reach a system equilibrium. The time-resolved quick XAS was introduced to discover the transient intermediate at the highly reactive stage. The quick XAS combined with density functional theory (DFT) calculation indicated the formation of Fe-O-As bonds, through condensation without redox, is energetically favored. Interestingly, nZVI can further facilitate the oxidation of As^{III} to a less toxic As^{V}=O species in the mid and long term. Moreover, the existence of this bonding will vary the sequestrating rate, and further down the reaction pathway.

1. Introduction

The availability of synchrotron radiation to the scientific community has revolutionized the way X-ray science is done in many disciplines, including environmental science. It allowed for the measurements of physical and chemical properties of materials, as well as their interactions with aqueous fluids and environmental contaminant ions under appropriate operating conditions. These analyses are indispensable for the understanding and modeling of reaction mechanisms and kinetics. The continuous development of third-generation synchrotron radiation sources allowed the execution of experiments requiring a high X-ray flux in a continuous interval, especially *in situ* monitoring under reactive conditions[1,2,3,4,5,6,7,8]. The possibility of performing time-resolved experiments using *in situ* devices is one of the most important methods for studying reaction pathways and obtaining a deeper knowledge of dynamic structure transition[9,10,11,12,13,14,15]. The present study targets the *in situ* sequestration of arsenic in aqueous solution under anaerobic conditions. This reaction is of enormous environmental relevance, since high levels of arsenic in groundwater have significant adverse effects on the environment, where groundwater is an important source of drinking water[16,17,18]. Therefore, finding an effective remediation method is critical.

The principal forms of arsenic in natural waters are arsenate (As^V) and arsenite (As^{III}). Diverse approaches for removing arsenic have been explored including various techniques such as coagulation, adsorption, ion exchange, membranes, photo-oxidation, reverse osmosis, nanofiltration, and conventional iron/manganese removal processes[19]. Besides these technologies, nanoscale zerovalent iron (nZVI), a highly reactive nanomaterial extensively evaluated for groundwater remediation and hazardous waste treatment, has been demonstrated as an effective method to remove arsenic in water under laboratory and field conditions[20,21,22]. Although in the last decade significant progress has been made toward understanding the structure and chemical composition of nZVI in the as-prepared state and after reaction[23,24,25], much less is known about *in situ* structural and chemical features and how they evolve in the course of a chemical reaction. It is generally believed that As^{III} and As^V is removed by adsorption of arsenic onto the passivating oxide layer of nZVI materials or coprecipitation with dissolved iron under high arsenic loadings[20,21,26,27]. Everlasting corrosion of nZVI in water provides a continuous source of surface sites for arsenic adsorption, which is considered a major advantage of nZVI method compared to conventional treatment using iron oxides. However, spectroscopic observation of arsenic-laden nZVI materials reveals that the immobilized arsenic is converted to different valence states from their aqueous forms, inferring arsenic redox transformations play an active factor in the remediation process.

Previous studies reported that As^{III} can be oxidized by active oxygen species with the presence of Fe^{II} in aerated water[28,29] or on the surfaces of Fe^{II}-goethite co-existence complex under anoxic conditions[30]. The application of X-ray photoelectron spectroscopy (XPS) has discovered oxidation of As^{III} to As^V, as well as As^{III} and As^V reduction in high nZVI-to-As mass ratios system[26,31,32,33,34]. Similar findings were detected by X-ray absorption spectroscopy (XAS) with a further probing depth, and in an *in situ* time-resolved XAS, introduced to examine the dynamic changes in the arsenic chemical state[35]. However, the time-scale was limited by the detector and the solution was also fixed in the reaction cell. Specially, most of the As^{III} in the solution can be captured by high dose loading nZVI in a very short time (less than 10 min). Undoubtedly, an understanding of this rapid transition and kinetics during the initial phase of the nZVI reaction with arsenic is of fundamental importance to enable the nZVI action against pollutants to be distinguished and to establish the nZVI reaction

model in groundwater. Few data have appeared in published studies to discuss the fundamental importance of the primary highly reactive species during the initial phase. The main problems lie in capturing the transient intermediate products and clear definition of the reaction mechanism.

Therefore, the aim of this study is to thoroughly elucidate the mechanism and kinetics of the reaction of nZVI with arsenic under anaerobic conditions at different time scales. An *in situ* flow cell with synchrotron-based XAS analysis was set up to effectively monitor the arsenic state under reactive conditions. To overcome the limitation of conventional XAS technique, the quick-scanning extended X-ay absorption fine structure (QEAXFS) was performed to reveal the transient reaction process at sub-second scale. Moreover, the combination of experimental results with computational chemistry enabled the initial reaction steps to be elucidated, clarifying the first unambiguous identification of the transit reactive intermediates. Considering the complexity and possible misinterpretation of the experimental observations on the nZVI reaction with arsenic, it would be highly beneficial to compare exact experimental data with theoretical calculations.

2. Experimental Section

2.1 Materials

Iron nanoparticles (nZVI) were synthesized by reacting 0.2 M sodium borohydride (NaBH$_4$, 98% purity, Scharlau) aqueous solution with 0.05 M ferric chloride (FeCl$_3$, 97%, Nacalai Tesque) solution which was prepared in an 80% v/v ethanol solution at ambient temperature with magnetic stirring and high-purity N$_2$ purging. Ferric iron is reduced by the borohydride according to the following reaction:

$$4Fe^{3+} + 3BH_4^- + 9H_2O \rightarrow 4Fe^0(s) + 3H_2BO_3^- + 12H^+ + 6H_2(g)$$
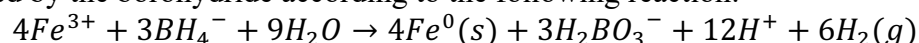
The as-synthesized nZVI was stored in a 95% ethanol solution in a sealed PTFE container at 4 °C prior to use.

2.2 *In Situ* Flow Cell Set-up

Stock solutions of 1000 mg/L As(III) and As(V) were prepared from NaAsO$_2$ and Na$_2$HAsO$_4$·7H$_2$O (>98.5%, Fluka), respectively. To eliminate dissolved O$_2$ as a potential oxidant in the solution and to simulate prevalent anoxic conditions encountered in groundwater environments, the solution was deoxygenated by sparging with N$_2$ for 30 min immediately before experiments. The nZVI and As reaction was performed in serum bottles containing 50 mL of As solution at 100 mg/L under anoxic conditions. Upon adding an appropriate amount of nZVI (0.1−5 g/L), the bottle was sealed with a PTFE-coated crew cap with three 1.6 mm hose connection, allowing mixture circulation and gas purging. Periodically, 1 mL of mixture were collected with a needle attached to a syringe and filtered through 0.22-μm syringe filters, and then transferred to a vial for analysis by ICP-OES (Inductively coupled plasma - optical emission spectrometry). The nZVI was dispersed by vigorous stirring at ambient temperature. *In situ* XAS studies revealing reaction pathway between arsenic and nZVI are implemented in a customized flow cell shown schematically in Figure 1. The *in situ* flow cell consists of a Teflon based main body (9*5.5*3 cm.) with a rectangular window (3*1*1 cm.) in the center and a pair of polymethyl methacrylate (PMMA) block and rubber gasket. The window with 1 cm thickness is designed to measure the transmission and fluorescence signal simultaneously (Fig. 1a). Briefly, mixtures are pumped out from the serum bottle by a peristaltic pump and flow into the Teflon based main body through a one screw-sealed bore opening on the top of the cell; meanwhile, the sample is pumped back to the serum bottle from another screw-sealed bore opening, forming a

flow loop for collecting homogeneous signal. The window was covered on two sides by Kapton® films supported on two PMMA block with a rubber gasket inserted on each side. Tightening of all eight screws on the cell compressed the PMMA blocks with Teflon based body well and ensured air-tight sealing without liquid leaking.
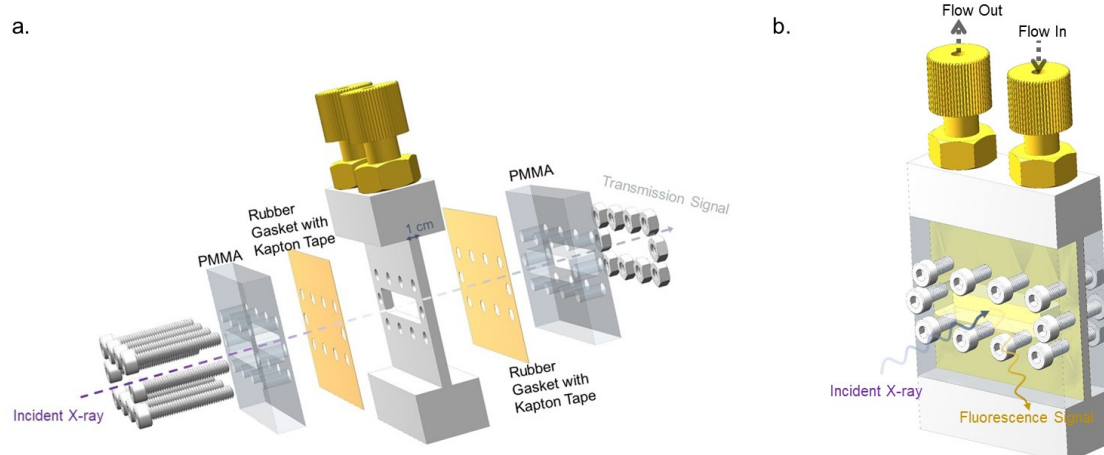

Figure 1. A schematic diagram of the in situ flow cell (a) before and (b) after assembly.

2.3 Synchrotron-based Spectroscopies

The *in situ* XAS measurements were conducted on the beamlines 07A1 of Taiwan Light Source (TLS) and 44A of Taiwan Photon Source (TPS) in National Synchrotron Radiation Research Center, Taiwan. The incident photon energy was calibarated using Fe foil and reagent grade sodium arsenate ($Na_2HAsO_4 \cdot 7H_2O$, Fluka) powder, respectively. 07A is a conventional X-ray absorption fine structure beamline and 44A equip the quick-scanning monochromator to provide the capability of spectrum collecting in sub-second time scale. Thus, the mid and long-term stage *in situ* XAS experiment was performed at 07A and the very early stage was carry out at 44A. Spectral processing and data analysis were conducted with the Demeter software package[36]. Linear combination fitting (LCF) of the sample spectra were used to identify the quantitative oxidation state information. The effect of X-ray irradiation on the As^{III} solution used herein was estimated by taking 90 min continuous scans of a pure As^{III} solution sample under X-ray illumination. There was no appreciable change in these time-series resultant spectra (Figure S1, SI).

Synchrotron-based experiments at soft X-ray energy regions were conducted on the beamlines 7.3.1 and 8.0.1 of Advanced Light Source (ALS) at Lawrence Berkeley National Laboratory. Soft XAS (sXAS) spectra were collected at bending magnet beamline 7.3.1 by measuring the total electron yield (TEY). The sXAS spectra have been normalized by the incident beam, which is measured by a clean gold mesh. Mapping of resonant inelastic X-ray scattering (mRIXS) experiments were performed in the iRIXS endstation at BL8.0.1. The undulator (U5) beamline 8.0.1 has a spherical grating monochromator providing a linearly polarized photon beam with an energy range from 80 eV to 1250 eV and a resolving power up to 5000. The mapping data were collected using an ultrahigh efficiency modular spectrometer with an excitation energy step of 0.2 eV. The final two-dimensional maps were obtained after energy calibration and normalization to collection time and incident X-ray beam flux, through a multi-step data process that has been detailed previously.

2.4 Characterization of Reacted Products

X-ray Photoelectron Spectroscopy (HR-XPS, ULVAC-PHI PHI QuanteraII). Samples

were measured in the C 1s, O 1s, As 2p, As 3d, and Fe 2p regions, which represented the major elements on the surface. All spectrum was calibrated by the binding energy of extrinsic carbon detected in the C1s region (284.6 eV).

2.5 DFT Calculations

DFT calculations of the nZVI nano clusters and their formation of complexes with $As^{III}(OH)_3$ were carried out using ORCA 4.1.2 on the high performance computing (HPC) cluster Lawrencium at the Lawrence Berkeley National Lab. Initial guesses of the Fe sites were based on crystal structure of Fe. Fe sites were set as Fe^{II} and terminated by OH groups suggested by Flip *et al*[37]. TD-DFT calculations were run on the optimized geometry to simulate the As *K*-edge XAS. Both geometry optimization and TD-DFT calculations were using B3LYP functional, def2-TZVP basis set and SARC/J auxiliary basis set, in PCM water.

3 Results and Discussion

3.1 *In situ* XAS at mid-term stage

The rates of arsenic sequestration by nZVI filings in the nitrogen system were investigated with different amounts of nZVI (0.1−5 g/L) loading. For experiments presented herein, an initial As^{III} concentration of 100 mg/L was used unless otherwise noted. Analysis of the arsenic concentration in the solution phase indicates that nZVI at a mass loading above 0.5 g/L sequestered more than 99% of the aqueous As^{III} species (Fig. 1a). With 2 g/L and higher dose of nZVI, aqueous As^{III} remaining in the solution is hard to detect by ICP-OES 10 min after the onset of the experiment. This sequestration process infers that nZVI can quickly interact with arsenic and effectively constrains arsenic during the ensuing period. However, only 50% of the As^{III} in the solution was sequestered by nZVI at a mass loading of 0.1 g/L after 24 h reaction. Although the As^{III} retention capacity should relate to doses of nZVI, the As^{III} sequestration curve of 0.1 g/L nZVI showed incomparable features to the other doses. It is worthwhile introduce a real-time monitoring method to probe the dynamic transition at different time scales and nZVI doses. The waterfall of time-series data (Fig 2b-e) happened in the *in situ* flow cell and was divided into three periods by the arrows. The time-resolved XANES spectra were collected at the frequency of approximately 7 min per scan. The energy positions of absorption peaks in the XANES region can be a fingerprint to distinguish As^{III} and As^{V}, which show obvious edge jump at 11870.7 and 11874.2 eV, respectively. The black arrow representing nZVI is added into the serum bottle and mixed with liquid As^{III}. In this time period, nZVI is isolated in the serum bottle by magnet, meaning all arsenic signals are contributed by aqueous phase. The yellow arrow indicates the mixture period where both nZVI and liquid are pumped out of the serum bottle and flow into the cell. When 0.1 g/L nZVI was added to As^{III} solution, there was no significant energy peak shift (Figure 2b) even during the mixture period, indicating no valence state change for arsenic species. In contrast to the reaction with low nZVI doses, the resultant data of high nZVI dose (> 0.5 g/L) series shows distinct regimes after adding nZVI. During the first period, the maximum absorption peak position located around 11870 eV represents the As^{III} species. Once high dose nZVI was added to As^{III} solution, the original absorption peak shifted to a higher energy position around 11874 eV (Figure 2c-e), showing a rapid oxidation of As^{III} to As^{V}. For nZVI at a mass loading higher than 0.5 g/L, less than 20% of As^{III} remained in solution after 60 min reaction, which means the majority of arsenic was sequestered by nZVI. While nZVI flowing into the cell, the presence of As^{V}, i.e., an obvious absorption

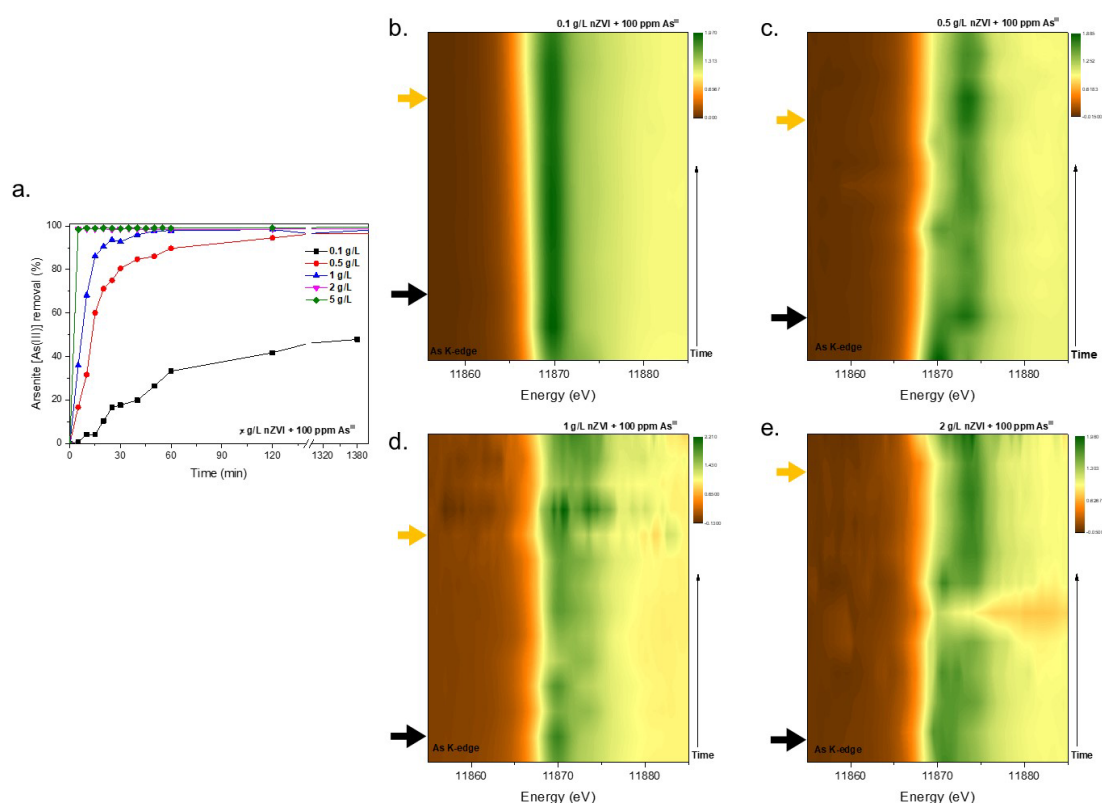threshold at 11874 eV, is more evident, revealing oxidation of As[III] both in liquid and solid phase.

Figure 2. (a) Removal of arsenic from solution by nZVI with time. Initial As[III] concentration was 100 ppm; nZVI dose was 0.1-5 g/L; reaction time was 24 h. Time-resolved As *K* edge XANES of *in situ* arsenic sequestration by nZVI at the mass loading of (b) 0.1, (c) 0.5, (d) 1, (e) 2 g/L; reaction time was 90 min. The black and yellow arrow in (b)-(e) represent pure liquid and mixture in flow cell, respectively.

3.2 *In situ* XAS at long-term stage

According to previous studies, although over 99% of the aqueous As[III] species are sequestered by nZVI, the arsenic-laden nanoparticles in the aqueous environment are still evolving. To observe the long-term structural transformation and changes in arsenic valence states, the real-time monitoring method was introduced to evaluate the dynamic transition of arsenic species both on liquid and solid phases at a time scale of 10 and 60 days. In comparison to the low dose nZVI, arsenic captured using a high dose of nZVI showed an obvious valence state change in the reaction pathway. Accordingly, the long-term experiment was investigated with 2 g/L of nZVI loading. Because the nZVI was already added to the As[III] solution and reacted for 10 and 60 days, there is only one yellow arrow in Fig.3 (a) and (b) to divide the waterfall data to two regimes, which are pure liquid and mixture period. As shown in Fig. 3 (a), a significant peak intensity around 11874 eV was observed at the first time period, indicating that As[V] is a dominant species in the liquid phase. However, the peak broadened to lower energy (11867- 11870 eV) rapidly over the subsequent mixture period, suggesting the reduction in the signal from arsenic-laden nanoparticles or the liquid around arsenic-laden nanoparticles. After circulating for another period, the signal was proceeding as homogeneous and dominated by As[V] again. Compared to monitoring the reaction at a time scale of 10 days, the spectra of 60-days' reaction in Fig. 3 (b) exhibited little change in the white line maxima. There were no appreciable changes in the spectra

beyond this time. As^{III} oxidation has been reported in the presence of goethite and other mineral surfaces with Fe^{II} species, and the reaction stopped as a specific As^V to As^{III} ratio was reached[30]. Reaching an equilibrium of the redox reaction between solid iron and arsenic is in accordance with the real-time monitoring reaction at a time scale of 60 days.
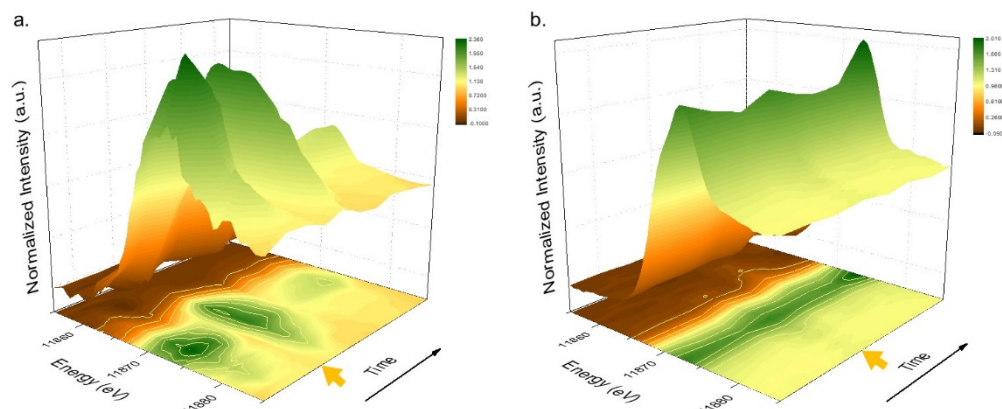

Figure 3. Time-resolved As K edge XANES of *in situ* arsenic sequestration by 2 g/L nZVI for (a) 10 and (b) 60 days. Yellow arrow indicates the mixture in the flow cell.

3.3 *Ex situ* characterization

To identify the arsenic valence state and structural transformation in solid phase, the concentrated precipitate from the real-time monitoring experiment was filtered through a syringe filter, then sealed between two pieces of Kapton polyimide film without drying for immediate XAS analysis. Figure 4 (a) shows the As K-edge XANES spectra of the concentrated precipitate collected from the real-time monitoring experiment at various reaction times and nZVI doses, and arsenopyrite (FeAsS) as a reference. The spectra show distinctive features in the main K edge (1s to 4p) transit which reveals the valence state for each sample. Except for the spectrum of 0.1 g/L, the main absorption peak of high nZVI dose react samples broadened at a high energy position around 11874 eV, indicating the presence of As^V. The valence state differences are more clearly seen in the first-derivative plots (Fig. 4b). The quantitative ratio of As^{III} and As^V shown in Fig 4c was calculated through linear combination fitting (LCF) by comparing white line features of two model compounds arsenate and arsenite for identifying arsenic valence states. For the solid collected at lowest (0.1 g/L) dose experiment, the amount of As^V on arsenic-laden nanoparticles is very low, which is consistent with the observation on real-time monitoring experiment (Fig. 2b). In contrast to the reaction at lowest dose, the ratio of As^{III} and As^V shows similarity in reactions at higher doses (0.5, 1 and 2 g/L). With increasing reaction time, the As^V became increasingly dominant in the spectra, whereas the ratio of the As^{III} and As^V calculated by LCF on arsenic-laden nanoparticles decreased to ca. 0.6 after 60 days. It should be noted that the absorption peak of samples collected at 2 g/L reaction after 10 days appeared to board at a lower energy position which is close to the white line maximum of FeAsS, especially clear in the first-derivative plot (Fig. 4b). Since the valence state of arsenic in FeAsS is −1, it is reasonable to infer that this highest dose (2 g/L) experiment resulted in arsenic with an anionic character after a 10-day reaction. A similar trend shown in the data from 90 min reaction, the main absorption peak broadened at lower and higher energy position, indicating both reduction and oxidation of As^{III} took place on arsenic-laden nanoparticles. To confirm the reduction of As^{III}, the surface-sensitive high-resolution

X-ray photoelectron spectroscopy (HR-XPS), which can provide valuable information about the valence states, was introduced to reveal the information of arsenic species on nanoparticle surfaces. Figure 4d and e shows As $3d$ XPS spectra of samples reacted with As^{III} solutions at mass loading of 2 g/L nZVI doses for 24 h and 10 days reaction. The as-reacted nZVI reveal the presence of multiple arsenic valence states, indicating As^V, As^{III}, and As^0 on the nZVI surfaces. Although the As^0 peak for 24 h reaction is not as relevant as that of 10 days reaction, the low amount of As^0 for 24 h is still detectable. The observation of As^V and As^0 on the nZVI sample, which were not present in the initial solution, indicates that As^{III} oxidation and reduction had occurred on arsenic-laden nanoparticles. In comparison to the high dose reaction, the spectrum of lower mass loading of 0.5 g/L nZVI dose for 24 h shows the absence of reduced arsenic species (Fig. 4e), despite the sequestration curve similarity (Fig. 2a). Notably, arsenic reduction was observed at the highest dose of nZVI (2 g/L), but not in 0.5 g/L samples. Similar to the previous study, this can be interpreted as a result of no As^0 on the arsenic-laden nanoparticles at a low dose system[33].
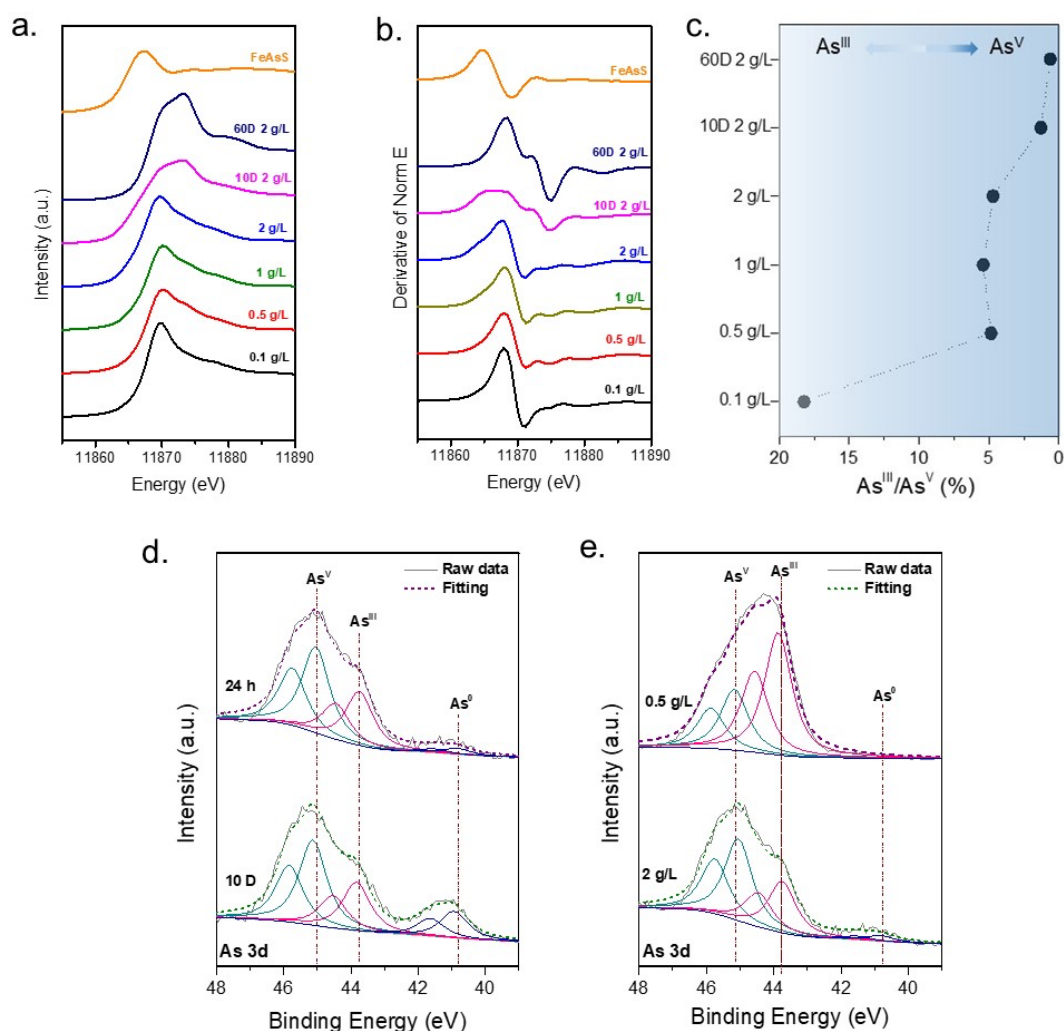

Figure 4. (a) As K-edge XANES spectra of samples collected from the *in situ* experiment without drying, and corresponding (b) first derivatives of the XANES spectra, and (c) ratio of the As^{III} and As^V calculated by LCF. As $3d$ XPS spectra comparison between (d) reaction time and (e) nZVI dose; reaction time was 24 h.

Figure 5a shows XAS at the O K-edge of 2 g/L samples after 24 h and 10-day reaction.

The feature in the pre-edge regions between ~ 525 and 530 eV exhibits a clear splitting peak, which originated from the transitions of hybridized states with t_{2g} and e_g orbital symmetry, respectively. In comparison to the sample reacted for 24 h, the sample after 10-day reaction shows a substantial increase of the relative ratio of t_{2g} to e_g. This feature of the pre-edge region is not only governed by the transition metal (TM) $3d$ components in the hybridized unoccupied orbital, but could arise from physisorbed oxygen, as well as lattice oxygen associated with possible precipitated oxide phases on the surface[38,39,40]. The variant ratio of t_{2g} to e_g can be assigned as surface hydroxyl groups replacement or ion exchange. Previous nZVI XPS studies lead to the conclusion that the E_h values in the solution phase, which is highly affected by the amount of nZVI, may be an indicator to the As^0 existence[30]. Because E_h represents the redox state of a solution, the appearance of As^0 on the reacted nZVI sample should initially form on the solid/liquid interface at this time scale. Conventional oxygen spectroscopy, especially O K-edge XPS and XAS have been extensively implemented for detecting, and quantifying, the oxygen redox reactions; nevertheless, they have suffered various technical issues from the shallow probe depth or entangled signals for achieving a reliable probe of oxygen redox states. High-efficiency full energy range mapping of resonant X-ray inelastic scattering (mRIXS) can further reveal the decay information at each sXAS excitation energy and be considered as a "further resolved" XAS decay process by providing detailed information on energy distribution of the fluorescence signals[41,42,43]. The mRIXS presented in Fig. 5b and c is technically further resolved XAS fluorescence signals along the emission energy (horizontal axis), and the horizontal integration of the mRIXS intensity corresponds to XAS-type signal channels. Besides the elastic line, strong mRIXS features around 525 eV emission energy (vertical axis) dominate the whole map but are separated along excitation energy into two regimes of a TM $3d$ character (528-534 eV) and TM $4s/p$ character (534-545 eV). In contrast to O K-edge XAS, there is no obvious splitting feature in pre-edge regime of mRIXS from the broad features around the 525 eV emission energy. Because the O K-edge XAS was collected in total electron signal mode, the electron penetration depth is limited within a few nanometers. The bulk-sensitive mRIXS provides a more integrated signal incorporated in the oxide matrix. In addition, the mRIXS signals around the characteristic 523.7 eV emission energy range get stronger with increasing the reaction time up to 10 days. Oxidations of either TMs or oxygen led to enhanced hybridization, in turn leading to stronger hybridization. The enhanced intensity could be naturally understood by considering that the system is oxidized upon while increasing the reaction time.
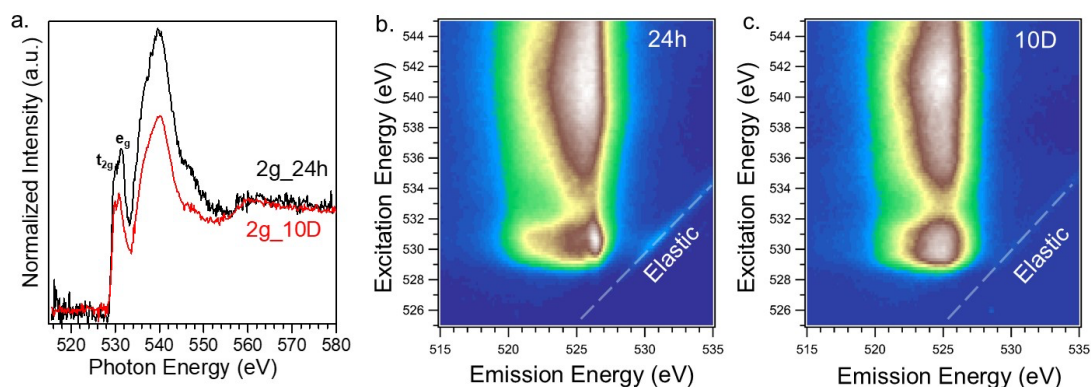

Figure 5. (a) O K edge spectra of 2 g/L samples after 24 h and 10-day reaction. O K-edge mRIXS of 2 g/L nZVI dose for (b) 24 h and (c) 10-day reaction. Color indicates the intensity distribution of the emitted photons, with blue presenting low intensity and white presenting high intensity.

3.4 *In situ* XAS at a very early stage

Prior results reported here reveal the reaction pathway of arsenic sequestration by nZVI at a time scale from minutes to days. It is worth noting that, regardless of the lowest nZVI dose, the sequestration curve in Fig. 2a shows the quickest reaction rate relative to later periods at a very early stage. With the aim to decipher the evolution of reaction at the early stage, QEXAFS is performed to discover the reaction process at sub-seconds scale. In order to obtain a better signal to background noise ratio, a relative high concentration of arsenic of 2000 mg/L was used for QEAXFS analysis. The reaction curve for high arsenic concentration sequestration (Fig. S2) is consistent with the behaviors shown in Figure 2a as long as the ratio of nZVI dose and concentration of arsenic is equivalent to the previous trial. Because of the rapid removal of aqueous As^{III} by nZVI observed in the solution phase analysis, the nZVI loading of 0.5 g/L was chosen to reflect primarily the process of arsenic transformation. Figure 5a shows the time-resolved quick XANES spectra of the mixture collected in the reaction flow cell. Although the scan frequency was approximately 0.5 sec per scan, the resultant spectra without normalization shown in Fig. 6a is integrated every 30 seconds to accentuate the pronounced decrease in the absorption intensity indicative of rapid transfer of the liquid As^{III} species to the solid phase. However, the spectra collected 150 secs after the initiation of the experiment exhibited little change in the absorption intensity, indicating another phase transformation stage. To shed light on the above-presented discrepancies between absorption intensity, the time-resolved series results with normalization and integration according to the absorption intensity variance are presented in Fig 6b. In this figure, all spectra within this time period are linearly aligned to compare the main absorption peak position, where there is a gradual but noticeable shift to lower energy while increasing reaction time. The relationship between the amount of energy shift and reaction times is shown in the inset of Fig. 6b. It should be noted that the peak shifts to a lower energy without broadening. This feature indicates that during the decreased absorption intensity stage, the starting arsenic species rapidly transform into an intermediate state with electron donation. Due to the strong sequestrated affinity of high dose nZVI to arsenic, the formation of high activity complexesis expected. Specially, there is no absorption peak shift for quick XAS experiment at 0.1 g/L nZVI loading (Fig. S3). It is likely that the reactive complexes form when the nZVI loading exceeds a certain level.
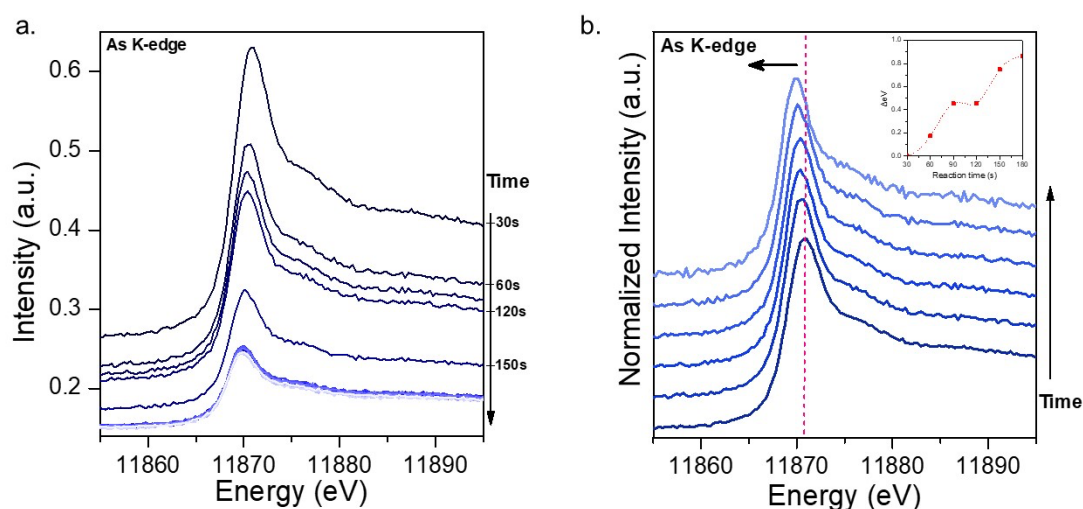

Figure 6. Time-resolved As *K* edge XAS of 0.5 g/L nZVI with ~ 0.5 sec per scan. Spectra (a) without and (b) normalization is integrated every 30 sec. Inset: The relationship between the amount of energy

3.5 DFT calculations

To elucidate the detailed reaction mechanism and identify the elementary reaction steps, DFT calculations were employed. In this study, we have tested the reactivity of both a mononuclear Fe site and a 4-Fe nano cluster, with the $As^{III}(OH)_3$ substrate. Prior experimental and theoretical studies by Flip *et al* suggested that in water, hydroxylated ferrous species is dominated at the nZVI surface even under anaerobic conditions, which we believe is the active species to react with arsenites[37]. Thus the initial guesses on the iron side were a $[Fe^{II}(OH)_4]^{2-}$ center and a tetrahedral 4-Fe^{II} cluster with OH groups respectively. The geometry of 4-Fe cluster was based on the Fe crystal structure (Fe_mp-150) and were terminated with OH groups[37] (Complex A in Figure 7). The xyz coordinates of Fe atoms was locked in space during geometry optimization. Total SCF energy differences of the reactants and products were used to evaluate the thermodynamics of the formation of the corresponding complexes. TD-DFT calculations were then applied to estimate the XAS absorption edge energy, and the shift of the edge energies were used to compare with experimental values (Figure 7).

3.5.1. $Fe^{II}(OH)_4$ with $As^{III}(OH)_3$.

To start with a simplified model, the condensation reaction between mononuclear $[Fe^{II}(OH)_4]^{2-}$ and $As^{III}(OH)_3$, forming an Fe-O-As bond with the loss of a water molecule, is shown by equation (1).

$$Fe^{II}(OH)_4 + As^{III}(OH)_3 \rightarrow (OH)_3Fe^{II} - O - As^{III}(OH)_2 + H_2O \tag{1}$$
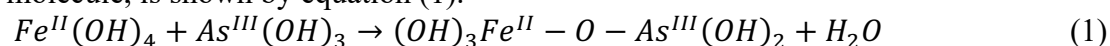
The ΔE of the forward reaction is -12.1 kcal/mol, suggesting that the Fe-O-As bond formation with the loss of water is energetically favored. The calculated As absorption edge energy decreased slightly from 11932.4 eV to 11932.2 eV. This small shift (0.2eV) is not likely to due to As redox, but from the change in the local chemical environment. As a reference, the calculated As absorption energy for the oxidized species $[As^V(OH)_4]^+$ is 11936.0 eV, which shifts 3.6 eV toward a higher energy, and is also a magnitude higher (Table 1).

Table 1 Calculated As absorption edge energy

As species[a]	Calculated As K-edge energy (eV)[b]	Relative shift (eV)
$As^{III}(OH)_3$	11932.4	0
$As^V(OH)_4^+$	11936.0	3.6
$O=As^V(OH)_3$	11935.6	3.2
$(OH)_2As^{III}-O-Fe^{II}(OH)_3$	11932.2	-0.2
Complex B	11932.2	-0.2
Complex C	11932.1	-0.3
Complex D	11932.0	-0.4
Complex E	11935.6	3.2

a. Complex B, C, D and E are the 4-Fe nano cluster models labeled in Figure 7. b. The absolute values from the DFT usually has some systematic error, thus it is the relative shift that is more important.

Table 2 Calculated ΔE of the reactions

Reaction[a]	Label	ΔE of the forward reaction (kcal/mol)

$As^{III}(OH)_3 + [Fe^{II}(OH)_4]^{2-}$ $\rightarrow (OH)_2\text{-}As^{III}\text{-}O\text{-}Fe^{II}(OH)_3 + H_2O$	(1)	-12.1
Complex A + $As^{III}(OH)_3$ $\rightarrow$ Complex B + H_2O	(2)	-17.8
Complex B $\rightarrow$ Complex C + H_2O	(3)	-4.6
Complex C $\rightarrow$ Complex D + H_2O	(4)	-4.1
$As(OH)_3 \rightarrow O=As(OH)_3$	(6)	x^b
Complex D $\rightarrow$ Complex E	(5)	x-27.8

a. Complex A, B, C, D and E are the 4Fe nano cluster models labeled in Figure 7. b. The detailed energy change is not known due to the fact that the reaction pathway is not fully understood, thus a value x is given here. However, the difference between reaction (5) and (6) can be determined. Reaction (5) has 27.8 kcal/mol more driving force toward the right.

3.5.2. 4-Fe nano cluster with $As^{III}(OH)_3$.
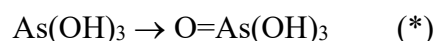The 4-Fe nano cluster can react with $As^{III}(OH)_3$ and forms up to three Fe-O-As bonds. The stepwise reactions are shown in Figure 7. The calculated ΔE of the forward reactions are -17.8 kcal/mol, -4.6 kcal/mol, and -4.1 kcal/mol respectively (Reaction 2, 3, 4, Table 2). The calculated As absorption edge energies are systematically shifted to a slightly lower energy every time an additional Fe-O-As bond is formed (Table 1).
Both the mononuclear Fe center and the 4-Fe nano cluster model show similar results that the formation of Fe-O-As bonds with loss of H_2O molecules (without any redox) are thermodynamically favored. The calculated As absorption edge energy shifts slightly to lower energy which is also consistent with experimental observations.

3.5.3. Follow up oxidation of As^{III} to As^{V}.
Experimental data shows that the As^{III} species are eventually oxidized to As^{V}, in the time range of hours or days (Fig. 2c-e and 3). Although the detailed mechanism is still not clear, we could still use DFT to evaluate the As=O bond strength[47]. Taking O=O bond strength in O_2 gas as 119 kcal/mol for reference, the O=As bond in O=As-nZVI is worth 109 kcal/mol. On the contrary, the O=As bond in regular $O=As(OH)_3$ is worth only 81 kcal/mol. There are differences in the nature of O-As bonds, resulting in different bond energies In O=As-nZVI (Complex E in Figure 7), the As-O(Fe) bonds (purple arrows) are weaker than its counterpart in $As(OH)_3$, due to the covalent O-Fe bonds on the other side (blue arrow), which leaves a stronger O=As bond (red arrows) to compensate this.
If we consider the two oxidation reactions with and without the presence of nZVI
$As(OH)_3 \rightarrow O=As(OH)_3$ (*)
$As\text{-}nZVI \rightarrow O=As\text{-}nZVI$ (**)
Although the directionality of each reaction cannot be determined, we still know that reaction (**) has ~28 kcal/mol more driving force towards the right hand side, makes it more likely to occur. We can also view this from a broader picture. Upon binding with a metal based nano cluster, the reduction potential decreases, which makes it an easier process to oxidize the As species.

To sum up, our DFT results showed that nZVI does not only adsorb the $As(OH)_3$ through the formation of As-O-Fe bonds in a thermodynamically favorable manner, but could facilitate the follow up oxidation process to As^{V} as well, which converts it to a less toxic species[48]. The high affinity between the Fe and As as well as the activation

of As by Fe could also provide valuable insights in understanding the toxicity mechanism of As species to enzymes.
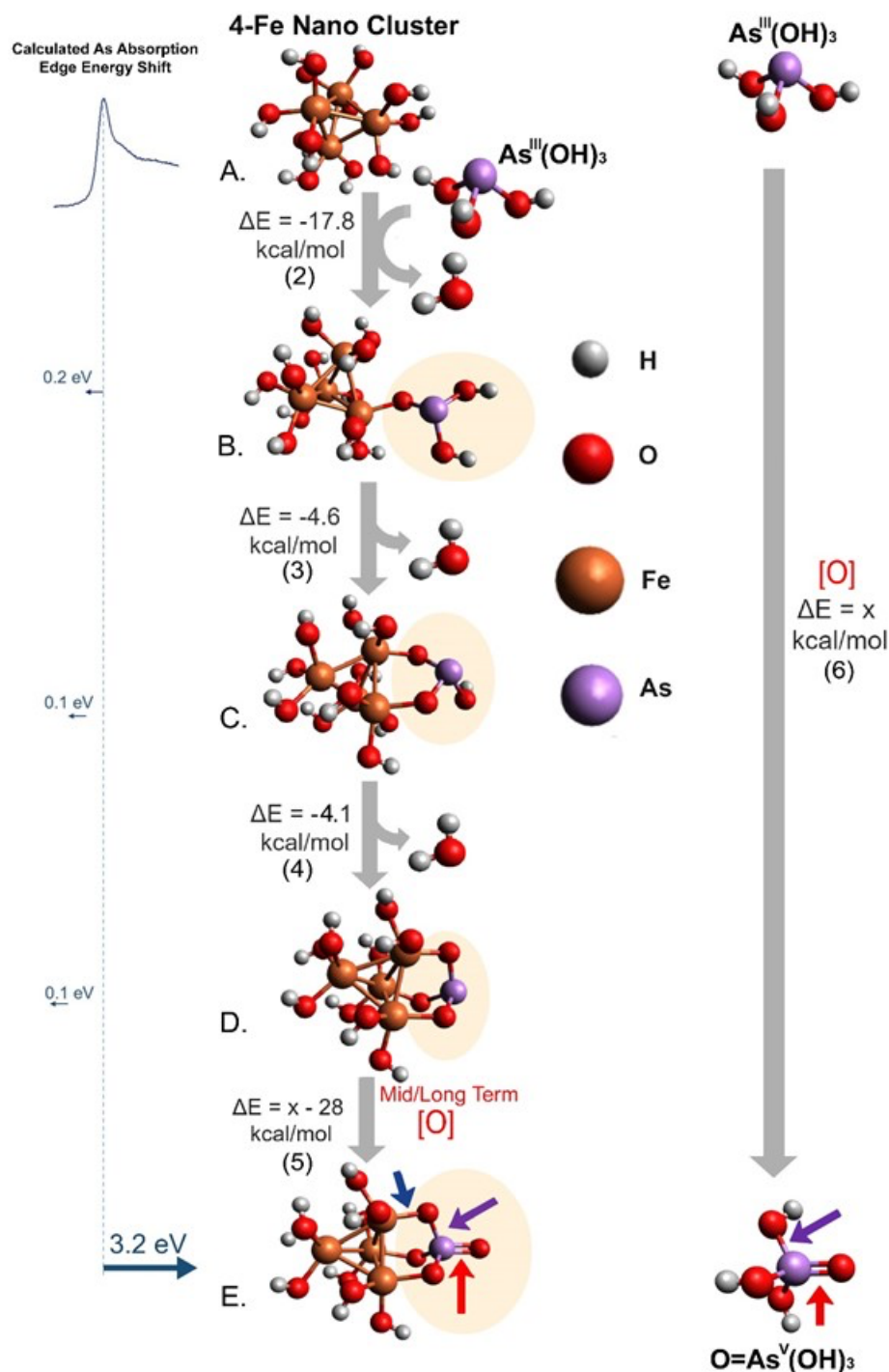

Figure 7. Proposed stepwise reactions of the 4-Fe cluster and arsenic based on the As *K*-edge QEXXAS spectra and DFT calculation. The complexes and reactions are labelled and will be referred in other places of this paper. The further oxidation step is based on the mid- and long-term *in situ* XAS results, and the calculated thermodynamics with and without the presence of nZVI are compared.

4. Conclusion
Herein, the real-time monitoring method was established to effectively study the

material state under reactive conditions. The experiment *in situ* investigated the complex mechanism of nZVI reaction with As^{III} under anaerobic conditions, revealing the valence state change of arsenic species, which can be used as evidence to understand the species evolution at the time scale from seconds to days. The dynamic changes in arsenic valence states at the mid-term stage (min to hours) suggest that an oxidation of As^{III} to As^{V} occurs both in the solid and liquid phase for the high nZVI dose system. By increasing the reaction time up to 60 days, As^{V} became the dominant species and the As^{III}/As^{V} ratio of arsenic-laden nanoparticles, calculated by LCF, decreased to ca. 0.6. The idea considering that the system is oxidizing upon is also supported by the oxygen K-edge mRIXS, which reveals hybridization intensity enhanced with increasing reaction time. Although there is arsenic with a reduction character at the highest dose (2 g/L) reaction, the reductive arsenic on the solid/liquid interface can be oxidized to As^{V} to reach the system equilibrium. For the first time, we identified the transient reaction intermediate at the highly reactive rate stage and thus most likely a crucial reductant for the rapid sequestration of arsenic by nZVI at high mass loading. The time-resolved As *K*-edge QEXAFS spectra shows a noticeable absorption peak shift from the original As^{III} to a lower energy position. According to the DFT calculation, the shift of the edge energies is possibly from the condensation reaction, which is also energetically favorable. Due to the condensation reaction, the highly reactive Fe-O-As bonds form and can be an oxidant for further redox activity. This is consistent with *in situ* XAS results at mid- and long-term time scale that As^{III} can be oxidized to As^{V} eventually. The effects of *in situ* monitoring solid/liquid reaction intermediates on the overall reactivity can be a promising subject of ongoing environmental water research.

References
1. Bordiga, et al. Reactivity of Surface Species in Heterogeneous Catalysts Probed by In Situ X-ray Absorption Techniques. *Chem. Rev.* **113**, 1736−1850 (2013).
2. Liu, et al. Distinct charge dynamics in battery electrodes revealed by in situ and operando soft X-ray spectroscopy. *Nat. Commun.* **4**, 2568 (2013).
3. Velasco-Velez, et al. The structure of interfacial water on gold electrodes studied by x-ray absorption spectroscopy. *Science* **346**, 831-834 (2014).
4. Zhang, et al. Revealing the Electrochemical Charging Mechanism of Nanosized Li_2S by in Situ and Operando X-ray Absorption Spectroscopy. *Nano Lett.* **17**, 5084-5091 (2017).
5. Wu, et al. Molecular-Scale Structure of Electrode–Electrolyte Interfaces: The Case of Platinum in Aqueous Sulfuric Acid. *J. Am. Chem. Soc.* **140**, 16237−16244 (2018).
6. Ye, et al. Dramatic differences in carbon dioxide adsorption and initial steps of reduction between silver and copper. *Nat. Commun.* **10**, 1875 (2019).
7. Ji, et al. Ultrahigh power and energy density in partially ordered lithium-ion cathode materials. *Nat. Energy* **5**, 213-221 (2020).
8. Kao, et al. In-situ/operando X-ray absorption spectroscopic investigation of the electrode/electrolyte interface on the molecular scale. *Surf. Sci.* **702**, 121720 (2020).
9. Kern, et al. Taking snapshots of photosynthetic water oxidation using femtosecond X-ray diffraction and spectroscopy. *Nat. Commun.* **5**, 4371 (2014).
10. Neppl, et al. Towards efficient time-resolved X-ray absorption studies of electron dynamics at photocatalytic interfaces. *Faraday Discuss.* **194**, 659-682 (2016).
11. Jacobs, et al. Exploring Chemistry in Microcompartments Using Guided Droplet Collisions in a Branched Quadrupole Trap Coupled to a Single Droplet, Paper

Spray Mass Spectrometer. *Anal. Chem.* **89**, 12511-12519 (2017).

12. Kern, et al. Structures of the intermediates of Kok's photosynthetic water oxidation clock. *Nature* **563**, 421 (2018).

13. Mahl, et al. Decomposing electronic and lattice contributions in optical pump – X-ray probe transient inner-shell absorption spectroscopy of CuO. *Faraday Discuss.* **216**, 414-433 (2019).

14. Chuang, et al. A design of resonant inelastic X-ray scattering (RIXS) spectrometer for spatial- and time-resolved spectroscopy. *J. Synchrotron Rad.* **27**, 695-707 (2020).

15. Loh, et al. Observation of the fastest chemical processes in the radiolysis of water. *Science* **367**, 179–182 (2020).

16. Nordstrom, et al. Worldwide Occurrences of Arsenic in Ground Water. *Science* **296**, 2143-2145 (2002).

17. Meharg, et al. Arsenic Contamination of Bangladesh Paddy Field Soils: Implications for Rice Contribution to Arsenic Consumption. *Environ. Sci. Technol.* **37**, 229–234 (2003).

18. Dittmar, et al. Arsenic Accumulation in a Paddy Field in Bangladesh: Seasonal Dynamics and Trends over a Three-Year Monitoring Period. *Environ. Sci. Technol.* **44**, 2925–2931 (2010).

19. Mohan, et al. Arsenic removal from water/wastewater using adsorbents—A critical review. *J. Hazard. Mater.* **142**, 1-53 (2007).

20. Su, et al. Arsenate and Arsenite Removal by Zerovalent Iron: Kinetics, Redox Transformation, and Implications for in Situ Groundwater Remediation. *Environ. Sci. Technol.* **35**, 1487–1492 (2001).

21. Kanel, et al. Removal of Arsenic(III) from Groundwater by Nanoscale Zero-Valent Iron. *Environ. Sci. Technol.* **39**, 1291–1298 (2005).

22. Yan, et al. Iron nanoparticles for environmental clean-up: recent developments and future outlook. *Environ. Sci.: Processes Impacts* **15**, 63-77 (2013).

23. Keenan, et al. Factors Affecting the Yield of Oxidants from the Reaction of Nanoparticulate Zero-Valent Iron and Oxygen. *Environ. Sci. Technol.* **42**, 1262–1267 (2008).

24. Greenlee, et al. Kinetics of Zero Valent Iron Nanoparticle Oxidation in Oxygenated Water. *Environ. Sci. Technol.* **46**, 12913−12920 (2012).

25. He, et al. Effect of Structural Transformation of Nanoparticulate Zero-Valent Iron on Generation of Reactive Oxygen Species. *Environ. Sci. Technol.* **50**, 3820−3828 (2016).

26. Bang, et al Chemical reactions between arsenic and zero-valent iron in water. *Water Res.* **39**, 763-770 (2005).

27. Morin, et al EXAFS and HRTEM Evidence for As(III)-Containing Surface Precipitates on Nanocrystalline Magnetite: Implications for As Sequestration. *Langmuir* **25**, 9119–9128 (2009).

28. Thoral, et al. XAS Study of Iron and Arsenic Speciation during Fe(II) Oxidation in the Presence of As(III). *Environ. Sci. Technol.* **39**, 9478-9485 (2005).

29. Ona-Nguema, et al. XANES Evidence for Rapid Arsenic(III) Oxidation at Magnetite and Ferrihydrite Surfaces by Dissolved O_2 via Fe^{2+}-Mediated Reactions. *Environ. Sci. Technol.* **44**, 5416–5422 (2010).

30. Amstaetter, et al. Redox Transformation of Arsenic by Fe(II)-Activated Goethite (α-FeOOH). *Environ. Sci. Technol.* **44**, 102–108 (2010)

31. Ramos, et al. Simultaneous Oxidation and Reduction of Arsenic by Zero-Valent Iron Nanoparticles: Understanding the Significance of the Core-Shell Structure.

J. Phys. Chem. C **113**, 14591-14594 (2009).

32. Yan, et al. Multi-tiered distributions of arsenic in iron nanoparticles: Observation of dual redox functionality enabled by a core–shell structure. *Chem. Commun.* **46**, 6995–6997 (2010).

33. Yan, et al. As(III) Sequestration by Iron Nanoparticles: Study of Solid-Phase Redox Transformations with X-ray Photoelectron Spectroscopy. *J. Phys. Chem. C* **116**, 5303−5311 (2012).

34. Tuček, et al. Zero-Valent Iron Nanoparticles Reduce Arsenites and Arsenates to As(0) Firmly Embedded in Core−Shell Superstructure: Challenging Strategy of Arsenic Treatment under Anoxic Conditions. *ACS Sustainable Chem. Eng.* **5**, 3027−3038 (2017).

35. Yan, et al. Intraparticle Reduction of Arsenite (As(III)) by Nanoscale Zerovalent Iron (nZVI) Investigated with In Situ X-ray Absorption Spectroscopy. *Environ. Sci. Technol.* 46, 7018−7026 (2012).

36. Ravel, et al. ATHENA, ARTEMIS, HEPHAESTUS: data analysis for X-ray absorption spectroscopy using IFEFFIT. *J. Synchrotron Rad.* **12**, 537-541 (2005).

37. Filip, et al. Anaerobic Reaction of Nanoscale Zerovalent Iron with Water: Mechanism and Kinetics. *J. Phys. Chem. C* **118**, 13817−13825 (2014).

38. Bora, et al. Evolution of an Oxygen Near-Edge X-ray Absorption Fine Structure Transition in the Upper Hubbard Band in α-Fe_2O_3 upon Electrochemical Oxidation. *J. Phys. Chem. C* **115**, 5619–5625 (2011).

39. Cao, et al. Low-Cost Synthesis of Flowerlike α-Fe_2O_3 Nanostructures for Heavy Metal Ion Removal: Adsorption Property and Mechanism. *Langmuir* 28, 4573−4579 (2012).

40. Mueller, et al. Redox activity of surface oxygen anions in oxygen-deficient perovskite oxides during electrochemical reactions. *Nat. Commun.* **6**, 6097 (2015).

41. Yang, et al. Anionic and cationic redox and interfaces in batteries: Advances from soft X-ray absorption spectroscopy to resonant inelastic scattering. *J. Power Sources* **389**, 188–197 (2018).

42. Zhuo, et al. Spectroscopic Signature of Oxidized Oxygen States in Peroxides. *J. Phys. Chem. Lett.* **9**, 6378−6384 (2018).

43. Wu, et al. Fingerprint Oxygen Redox Reactions in Batteries through High-Efficiency Mapping of Resonant Inelastic X-ray Scattering. *Condens. Matter* **4**, 5 (2019).

44. Gent, et al. Coupling between oxygen redox and cation migration explains unusual electrochemistry in lithium-rich layered oxides. *Nat. Commun.* **8**, 2091 (2017).

45. Xu, et al. Elucidating anionic oxygen activity in lithium-rich layered oxides. *Nat. Commun.* **9**, 947 (2018).

46. Hong, et al. Metal–oxygen decoordination stabilizes anion redox in Li-rich oxides. *Nat. Mater.* **18**, 256-265 (2019).

47. Ha, et al. Sulfur K-Edge X-ray Absorption Spectroscopy and Density Functional Theory Calculations on Monooxo Mo^{IV} and Bisoxo Mo^{VI} Bis-dithiolenes: Insights into the Mechanism of Oxo Transfer in Sulfite Oxidase and Its Relation to the Mechanism of DMSO Reductase. *J. Am. Chem. Soc.* **136**, 9094-9105 (2014).

48. Aposhian, et al. Oxidation and detoxification of trivalent arsenic species. *Toxicol. Appl. Pharmacol.* **193**, 1-8 (2003).

Author Information:
These authors contributed equally: Li Cheng Kao, Yang Ha.

Affiliations
Advanced Light Source, Lawrence Berkeley National Laboratory, Berkeley, California 94720, USA
Li Cheng Kao, Yang Ha, Xuefei Feng, Feipeng Yang, Wanli Yang, Jinghua Guo

Department of Geosciences, National Taiwan University, Taipei 106, Taiwan.
Wan Jou Chang, Sofia Ya Hsuan Liou

National Synchrotron Radiation Laboratory, University of Science and Technology of China, Hefei, Anhui 230026, P. R. China
Yifan Ye

National Synchrotron Radiation Research Center Hsinchu 300, Taiwan
Jeng-Lung Chen, Chih-Wen Pao

Molecular and Cellular Biology: Biochemistry, University of California, Berkeley, CA 94720, USA
Catherine Zhu

Department of Chemistry and Biochemistry, University of California, Santa Cruz, CA 95064, USA
Jinghua Guo